Science Bulletin 64 (2019) 1262–1271

Contents lists available at ScienceDirect

Science Bulletin

journal homepage: www.elsevier.com/locate/scib

Science Bulletin
www.scibull.com

Article

# Surface sulfurization activating hematite nanorods for efficient photoelectrochemical water splitting

Lianlian Mao [a], Yu-Cheng Huang [b], Yanming Fu [a], Chung-Li Dong [b,*], Shaohua Shen [a,*]

[a] International Research Center for Renewable Energy, State Key Laboratory of Multiphase Flow in Power Engineering, Xi'an Jiaotong University, Xi'an 710049, China
[b] Department of Physics, Tamkang University, Tamsui 25137, Taiwan, China

ARTICLE INFO

*Article history:*
Received 7 June 2019
Received in revised form 2 July 2019
Accepted 8 July 2019
Available online 12 July 2019

*Keywords:*
Photoelectrochemical
Water splitting
Hematite nanorods
Photoanodes
Surface sulfurization

ABSTRACT

Surface treatment is an effective method to improve the photoelectrochemical (PEC) performance of photoelectrodes. Herein, we introduced a novel strategy of surface sulfurization to modify hematite ($\alpha$-$Fe_2O_3$) nanorods grown in an aqueous solution, which triggered encouraging improvement in PEC performances. In comparison to the solution-grown pristine $\alpha$-$Fe_2O_3$ nanorod photoanode that is PEC inefficient and always needs high temperature (>600 °C) activation, the surface sulfurized $\alpha$-$Fe_2O_3$ nanorods show photocurrent density increased by orders of magnitude, reaching 0.46 mA $cm^{-2}$ at 1.23 V vs. RHE (reversible hydrogen electrode) under simulated solar illumination. This improvement in PEC performances should be attributed to the synergy of the increased carrier density, the reduced surface charge carrier recombination and the accelerated water oxidation kinetics at the $\alpha$-$Fe_2O_3$/electrolyte interface, as induced by the incorporation of S ions and the formation of multi-state S species (Fe-$S_x$-$O_y$) at the surface of $\alpha$-$Fe_2O_3$ nanorods. This study paves a new and facile approach to activate $\alpha$-$Fe_2O_3$ and even other metal oxides as photoelectrodes for improved PEC water splitting performances, by engineering the surface structure to relieve the bottlenecks of charge transfer dynamics and redox reaction kinetics at the electrode/electrolyte interface.



## 1. Introduction

The excessive exploitation of traditional energy has caused extremely serious environmental problems, which has make the human society realize the urgency of developing and utilizing clean and renewable energy [1]. Since Fujishima and Honda [2] discovered water photolysis on $TiO_2$ in 1972, photoelectrochemical water splitting has been considered as a promising route to solve these problems, as it can produce clean and recyclable energy of $H_2$ from water by solar light [3]. Until now, except for $TiO_2$ [4], various oxide semiconductors have been widely investigated as photoanodes for solar water splitting, like $Fe_2O_3$ [5], $BiVO_4$ [6], and $WO_3$ [7]. Among them, hematite ($\alpha$-$Fe_2O_3$) has been receiving increasing attention as photoanode for PEC water oxidation, given its inherent advantages, such as earth abundance, non-toxicity, good stability and low cost [8,9]. Moreover, given its favorable optical band gap (~2.2 eV) for solar light absorption, its theoretical solar-to-hydrogen efficiency could reach as high as 16.8% [10]. However, the actual efficiencies achieved yet are still much lower than the theoretical value, mainly due to the very short lifetime of photo-generated charge carriers (<10 ps) and short hole diffusion length (2–4 nm) as well as the sluggish surface water oxidation reaction kinetics, which gives rise to a high recombination rate of photo-generated charge carriers in the bulk and at the surface of $\alpha$-$Fe_2O_3$ photoanodes [11].

Hitherto, enormous efforts have been made to modify $\alpha$-$Fe_2O_3$ photoanodes to overcome these bottlenecks for the enhanced PEC water splitting performances. For example, doping of foreign elements, such as Al [12], Ti [13], Zn [14], Si [15], and Sn [16], etc., has been evidenced effective to increase the charge density and then improve the electronic conductivity in $\alpha$-$Fe_2O_3$ photoanodes for efficient charge transfer in bulk and thus enhanced PEC activities [9,17]. Nanostructure design, an effective approach to manipulating the morphology and dimension at nanometer scale (e.g., nanorods, nanotubes, nanowires, etc.) [18–20], have been applied to compensate the short hole diffusion length in $\alpha$-$Fe_2O_3$ for the timely charge transfer from bulk to surface. Despite of these achievements, the crucial drawback of the high recombination rate of surface trapped holes still remains at the surface of $\alpha$-$Fe_2O_3$ photoanodes, which greatly limits the further enhancement in PEC

* Corresponding authors.
*E-mail addresses:* cldong@mail.tku.edu.tw (C.-L. Dong), shshen_xjtu@mail.xjtu.edu.cn (S. Shen).

https://doi.org/10.1016/j.scib.2019.07.008
2095-9273/

performances. Thus, surface treatment would be of great necessity and also effectiveness to improve the PEC activities by inhibiting surface electron-hole recombination and/or accelerating surface water oxidation reaction kinetics [16,21,22]. It has been well demonstrated that various cocatalysts those are supposed to provide the active sites and sequentially accelerate four-electron water oxidation reaction kinetics have been widely used for the surface modification of α-$Fe_2O_3$ photoanodes for efficient PEC water splitting [23,24]. Otherwise, some wide band gap metal oxides, such as $Ga_2O_3$ [21], $Al_2O_3$ [25], $TiO_2$ [26], and ZnO [27], acting as passivation layers, have been deposited on the surface of α-$Fe_2O_3$ photoanodes to eliminate the surface trap states for reduced charge recombination. With surface treated by acids like HCl, HCOOH, $H_3PO_4$, or $H_3BO_3$ [28,29], α-$Fe_2O_3$ photoanodes also exhibited increased PEC performances, due to the elimination of surface trap states and then the inhibited surface electron-hole recombination. For example, Lan et al. [29] reported that a simple $H_3BO_3$ treatment process could significantly improve the performance of the obtained α-$Fe_2O_3$ photoanodes with a largely lowered onset potential and a highly increased photocurrent density, as B can effectively passivate $Fe^{IV}$ defects, subsequently inhibiting the surface charge carrier recombination.

Herein, as an alternative demonstration of surface treatment, we introduced a facile and effective approach to modify the surface structures of α-$Fe_2O_3$ photoanode via surface sulfurization of the hydrothermally grown β-FeOOH nanorods in a thioacetamide (TAA) aqueous solution with different concentrations (0.05, 0.2, 0.5 mol $L^{-1}$), followed by a low-temperature (<600 °C) annealing in argon (Ar) atmosphere. The obtained surface sulfurized α-$Fe_2O_3$ nanorods, named as Fe-S(0.05), Fe-S(0.2) and Fe-S(0.5), respectively, showed significant improvements in PEC performance with photocurrent density increased by orders of magnitude as well as favorable long-term PEC stability, as compared to the bare α-$Fe_2O_3$. It was proposed that the surface incorporation of S ions could increase charge carrier density, facilitating charge carrier transfer and separation, and the formed multi-state S species (Fe-$S_x$-$O_y$) reduce surface electron–hole recombination and accelerate water oxidation kinetics at the electrode/electrolyte interface, which synergistically improved the PEC properties of α-$Fe_2O_3$ nanorods for water oxidation. Encouragingly, this study demonstrates a simple, economical and effective surface treatment approach to activate α-$Fe_2O_3$ photoanodes for efficient and stable solar water splitting, which we believe can be also applied to other nanostructured metal oxides and oxyhydroxides used in different fields, such as photodetectors, solar cells, etc.

## 2. Experimental

### 2.1. Synthesis of α-$Fe_2O_3$ nanorods

The α-$Fe_2O_3$ nanorods were grown on fluorine doped tin oxide (FTO, Nippon Sheet Glass, TEC-14, 14 Ω $sp^{-1}$) coated glass substrates via an aqueous solution approach developed by Vayssieres et al. [30] with minor modification. Typically, ferric chloride ($FeCl_3{\cdot}6H_2O$, ≥99.0%, 0.15 mol $L^{-1}$), sodium nitrate ($NaNO_3$, ≥99.0%, 1 mol $L^{-1}$) and hydrochloric acid (HCl, 36%–38%, 50 μL) were mixed in an aqueous solution (20 mL), then two back to back pieces of FTO glass were placed in a glass vial with cap-sealed and leaned against the inner wall. After heating at 100 °C for 24 h in a regular oven, the obtained yellowish β-FeOOH film was rinsed with deionized water and dried, then annealed in air atmosphere at 550 °C for 2 h with ramping rate of 5 °C $min^{-1}$, to obtain the bare α-$Fe_2O_3$ photoanode, denoted as Fe(Air). The β-FeOOH film was also annealed in argon (Ar) atmosphere at 550 °C for 2 h to obtain α-$Fe_2O_3$ as reference, denoted as Fe(Ar).

### 2.2. Synthesis of surface sulfurized α-$Fe_2O_3$ nanorods

To obtain surface sulfurized α-$Fe_2O_3$ nanorods, the as-grown β-FeOOH films were immersed in thioacetamide (TAA) aqueous solutions with different concentrations (0.05, 0.2, 0.5 mol $L^{-1}$) for 30 s and dried, and surface sulfurized α-$Fe_2O_3$ photoanodes, denoted as Fe-S(0.05), Fe-S(0.2) and Fe-S(0.5), respectively, were then obtained via an Ar annealing process as described above.

### 2.3. Characterizations

The morphology of the samples was observed by a scanning electron microscope (SEM, JEOL JSM-7800F) at an accelerating voltage of 3 kV, and a transmission electron microscope (TEM, FEI Tecnai G2 F30) at an accelerating voltage of 300 kV. The crystal structure of the samples was examined by X-ray diffraction (XRD) using a PANalytical X'pert MPD Pro X-ray diffractometer with Ni-filtered Cu Kα (λ = 1.5406 Å) irradiation. The phase of the samples was identified by Raman scattering on a Jobin Yvon Lab-RAM HR spectrometer using an argon ion laser with 514.5 nm irradiation at 20 mW. The optical absorption of the samples was measured by a Hitachi U-4100 UV–vis-near-IR spectrophotometer. The chemical composition was investigated by X-ray photoelectron spectroscopy (XPS, Kratos Axis Ultra DLD) with monochromatic Al Kα irradiation. The C1s line of adventitious carbon was calibrated to 284.8 eV to compensate for the charge effect. The XAS at Fe and S K-edge were performed at hard X-ray beamline (BL 17C) and tender X-ray beamline (BL16A), respectively. The XAS at Fe L-edge was made at soft X-ray beamline (BL20A). An 1.5 AM solar simulator was used to collect the XAS spectra under illuminated condition.

### 2.4. Photoelectrochemical (PEC) and electrochemical measurements

The PEC measurements were conducted by a three-electrode cell connected to an electrochemical workstation (CHI 760D) in 1 mol $L^{-1}$ NaOH (pH 13.6) aqueous solution. The prepared photoanodes acted as the working electrodes, Pt and Ag/AgCl were used as the counter and the reference electrode, respectively. The photoanodes with exposed area fixed at 0.785 $cm^2$ were irradiated with a solar simulator (300 W Xe lamp) adjusted to be 100 mW $cm^{-2}$ at the sample position through an AM 1.5 G filter. The potentials obtained vs. Ag/AgCl electrode were converted to reversible hydrogen electrode (RHE) according to Nernst equation:

$$E_{RHE} = E_{Ag/AgCl} + 0.059\ pH + E^{o}_{Ag/AgCl}, \quad (1)$$

where $E_{RHE}$ is the converted potential vs. RHE, $E_{Ag/AgCl}$ is the experimentally measured potential vs. Ag/AgCl (saturated KCl), and $E^{o}_{Ag/AgCl}$ is 0.1976 V at 25 °C.

The incident photon to current conversion efficiency (IPCE) was calculated according to the following equation:

$$IPCE(\lambda) = \frac{1240 \times J(\lambda)}{P \times \lambda}, \quad (2)$$

where $P$ is the power intensity (mW $cm^{-2}$) and $\lambda$ is the wavelength (nm) of the incident monochromatic light, $J(\lambda)$ is the photocurrent density (mA $cm^{-2}$) under the irradiation of monochromatic light. IPCE measurements were performed by a computer controlled monochromator with a lock-in amplifier for photocurrent detection under applied potential of 0.23 V vs. Ag/AgCl, and a radiometer/photometer was used to measure the absolute intensity of the incident light from the monochromator.

The electrochemically active surface areas (ECSAs) [25] were determined by the electrochemical double-layer capacitances ($C_{dl}$) via cyclic voltammetry (CV) plots obtained at different scan

rates of 10, 25, 50, 75, 100, 125, 150, 175 and 200 mV $s^{-1}$ in the dark, with sweep potential range from 0.9 to 1.1 V vs. RHE in 1 mol $L^{-1}$ NaOH. The $C_{dl}$ and ECSA can be calculated by the following equations [31]:

$$C_{dl} = \frac{(J_a - J_c)/2}{v}, \quad (3)$$

where $J_a$ and $J_c$ are the positive and negative scan current at 0 V (vs. Hg/HgO), $v$ is the scan rate.

$$ECSA = \frac{C_{dl}}{C_s}, \quad (4)$$

where $C_s$ is the specific capacitance, which is 40 μF $cm^{-2}$ in 1 mol $L^{-1}$ NaOH [31].

Mott-Schottky (M–S) measurements were performed in the dark at 1 kHz frequency with the same three-electrode configuration in 1 mol $L^{-1}$ NaOH electrolyte based on the following equation:

$$\frac{1}{C^2} = \frac{2}{e\varepsilon\varepsilon_0 N_d}\left[(V - V_{fb}) - \frac{kT}{e}\right], \quad (5)$$

where $C$ is the space charge capacitance, $e$ is the electron charge ($1.602 \times 10^{-19}$ C), $\varepsilon$ is the dielectric constant of α-$Fe_2O_3$ (80) [32], $\varepsilon_0$ is the vacuum permittivity ($8.854 \times 10^{-14}$ F $cm^{-1}$), $N_d$ is the carrier density, $V$ is the applied potential at the electrode, $V_{fb}$ is the flat band potential obtained from the horizontal axis intercept of M–S plots, $k$ is the Boltzmann's constant ($1.38 \times 10^{-23}$ J $K^{-1}$), $T$ is the absolute temperature (298 K). The slopes from the M–S plots have a linear relationship, which were used to estimate the carrier density ($N_d$) in semiconductors, according to the following equation:

$$N_d = \left(\frac{2}{e\varepsilon\varepsilon_0}\right)\left[\frac{d\left(\frac{1}{C^2}\right)}{dV}\right]^{-1}. \quad (6)$$

Considering the ECSA, the true charge density ($N_{d,\ true}$) can be estimated by

$$N_{d,\ true} = \frac{N_d}{ECSA}. \quad (7)$$

The width of the space charge layer ($W_{sc}$) was obtained by the equation [33]:

$$W_{sc} = \sqrt{\frac{2\varepsilon\varepsilon_0(V - V_{fb})}{eN_d}}. \quad (8)$$

The open-circuit photovoltage was calculated by the difference of open-circuit potentials between dark and light:

$$V_{ph} = V_{oc,\ dark} - V_{oc,\ light}, \quad (9)$$

where $V_{oc,\ dark}$ and $V_{oc,\ light}$ are the open-circuit potentials in the dark and light, respectively. $V_{ph}$ is the corresponding photovoltage. $V_{oc,\ light}$ is tested under simulated 1 sun (AM 1.5 G, 100 mW $cm^{-2}$).

The lifetime of photo-generated charge carriers ($\tau_n$) was determined with open-circuit potential by the following equation [34]:

$$\tau_n = \frac{kT}{e}\left(\frac{dV_{oc}}{dt}\right)^{-1}. \quad (10)$$

To further evaluate the charge transfer processes in α-$Fe_2O_3$ nanorod photoanodes, the charge carrier separation and injection efficiencies ($\eta_{separation}$ and $\eta_{injection}$) were quantified using the equations reported by Dotan et al. [35]:

$$J_{H_2O} = J_{absorbed} \times \eta_{separation} \times \eta_{injection}, \quad (11)$$

$$J_{Na_2SO_3} = J_{absorbed} \times \eta_{separation}, \quad (12)$$

where $J_{H_2O}$ is the photocurrent density measured in 1 mol $L^{-1}$ NaOH electrolyte; $J_{Na_2SO_3}$ is the photocurrent density measured with 0.5 mol $L^{-1}$ $Na_2SO_3$ added in the same electrolyte; $J_{absorbed}$ is the rate of photon absorption expressed as a current density; $\eta_{separation}$ is the charge separation efficiency in the bulk; $\eta_{injection}$ is the charge injection efficiency from α-$Fe_2O_3$ to electrolyte. It is well accepted that charge injection efficiency becomes 100% at the presence of hole scavenger ($Na_2SO_3$) in the electrolyte [36]. Thus, the charge injection efficiency into water is achieved by $J_{H_2O}/J_{Na_2SO_3}$ and the charge separation efficiency is obtained by $J_{Na_2SO_3}/J_{absorbed}$.

Electrochemical impedance spectroscopy (EIS) measurements with a sinusoidal perturbation amplitude of 10 mV at frequency from 100 kHz to 0.1 Hz were performed with the three-electrode configuration at 0.23 V vs. Ag/AgCl in 1 mol $L^{-1}$ NaOH electrolyte under illumination.

## 3. Results and discussion

In this study, α-$Fe_2O_3$ nanorods were explored as the typical nanostructured photoanodes with shortened charge transfer distance and directed charge carrier transport pathway in the one-dimensional nanorod structure. The surface sulfurized α-$Fe_2O_3$ nanorods were obtained through a facile solution based sulfurization process using TAA as sulfur precursor, followed by a low-temperature (550 °C) annealing process. As scanning electron microscope (SEM) images shown in Fig. 1, both the bare and surface sulfurized α-$Fe_2O_3$ photoanodes have very similar morphology of nanorod arrays vertically grown on the fluorine doped tin oxide (FTO) substrates with thickness of ~600 nm and diameter ranging from ~30 to ~50 nm, corresponding well with the previous observations [37,38], the same height with Fe(Air) as shown in Fig. S1 (online). Further analysis in the X-ray diffraction (XRD) patterns (Fig. S2 online) and Raman spectra (Fig. S3 online) demonstrates almost the same phase and crystal structures for all the bare and surface sulfurized α-$Fe_2O_3$ nanorods, which speculates that TAA sulfurization may only act on the superficial region of these obtained α-$Fe_2O_3$ nanorods.

X-ray photoelectron spectroscopy (XPS) measurements were conducted to characterize the surface chemical compositions of the photoanodes. As shown in Fig. S4 (online), the Fe $2p_{3/2}$ and Fe $2p_{1/2}$ peaks of the bare and surface sulfurized α-$Fe_2O_3$ photoanodes show very similar profiles with binding energies of ~711.0 and ~724.1 eV, well corresponding to $Fe^{3+}$ in α-$Fe_2O_3$ [39]. In contrast to the bare α-$Fe_2O_3$ nanorods, e.g., Fe(Ar) (Fig. S5 online), the S 2p signals can be clearly observed for the surface sulfurized α-$Fe_2O_3$ films (Fig. 2a). The peaks at 159.4 and 168.6 eV should be attributed to $S^{2-}$ [40] and $SO_4^{2-}$ [41,42], respectively, while the observed signals locating at 164.6 eV could be related to the polysulfides ($S_n^{2-}$, $2 < n < 8$) [43] caused core hole effects [44,45]. Fig. 2b shows the O 1 s signals for the bare and surface sulfurized α-$Fe_2O_3$ photoanodes. The main peak at around 529.8 eV is the characteristic peak attributed to lattice oxygen, while the small peak at around 531.4 eV should be related to the surface absorbed hydroxyl group, as similarly observed for α-$Fe_2O_3$ in Ref. [46]. Notably, for the surface sulfurized α-$Fe_2O_3$ nanorods, the O 1 s signals at 529.8 eV shift to higher binding energy by ~0.1 eV, which should be related to the introduction of S ions at the surface of α-$Fe_2O_3$ nanorods. As supposed that the Ar annealing process might drive S ions to diffuse into the Fe-O lattice and replace O atoms during the formation of hematite structure [47], the introduced S element with lower electronegativity than O element would alter the electron cloud distribution and increase the electron density around O atoms, leading to the shift of O 1s XPS peaks to higher binding energies, which thus well evidences the successful surface sulfurization of α-$Fe_2O_3$ nanorods. All these

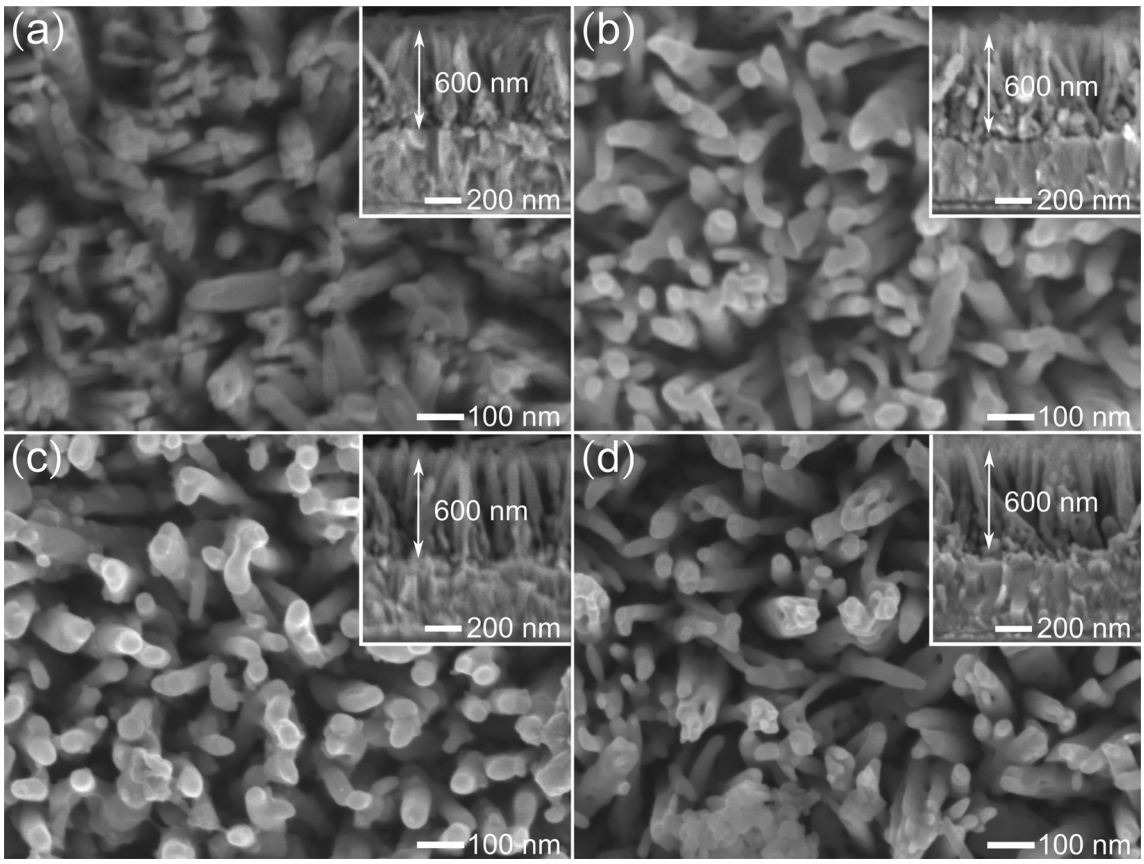


**Fig. 1.** SEM images of bare and surface sulfurized α-$Fe_2O_3$ nanorods. (a) Fe(Ar), (b) Fe-S(0.05), (c) Fe-S(0.2), and (d) Fe-S(0.5).

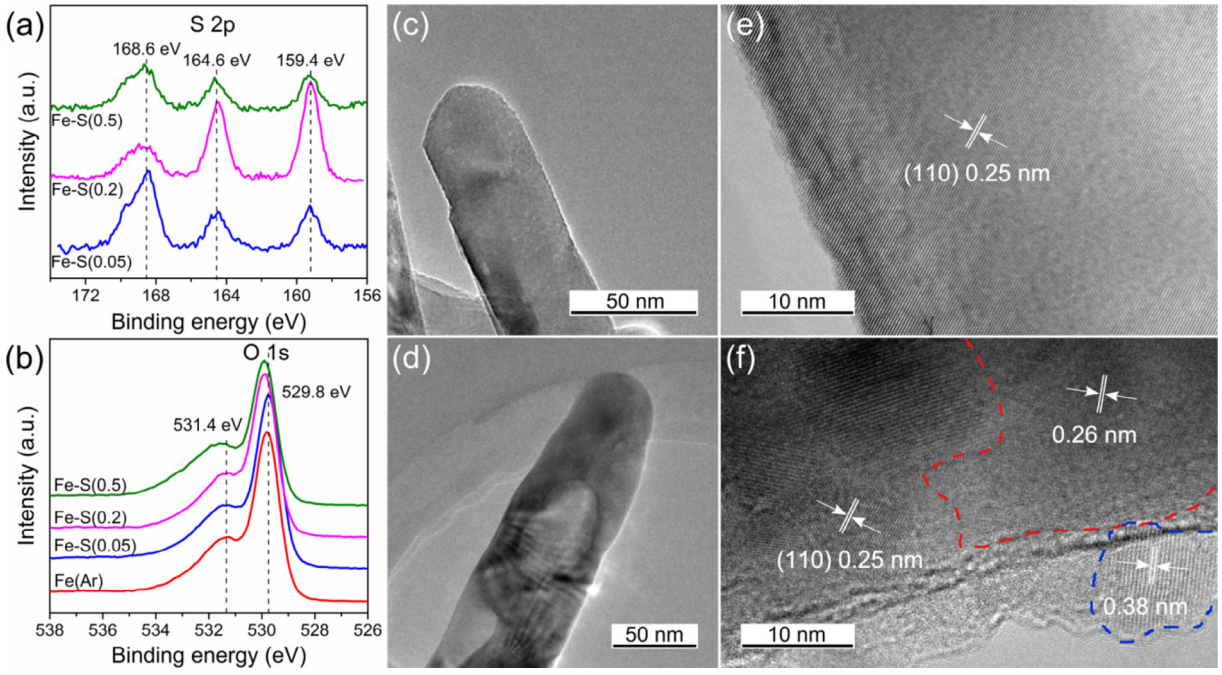


**Fig. 2.** (Color online) XPS spectra of Fe(Ar), Fe-S(0.05), Fe-S(0.2), and Fe-S(0.5): (a) S 2p and (b) O 1s profiles. TEM images of (c) Fe(Ar) and (d) Fe-S(0.2); HRTEM images of (e) Fe(Ar) and (f) Fe-S(0.2).

observations suggest the successful surface sulfurization of α-$Fe_2O_3$ nanorods and the possible formation of multi-state S species (Fe-$S_x$-$O_y$) at the nanorod surface, and the S surface content is calculated to be ~2.35 at% for Fe-S(0.2) by analyzing the XPS peak areas.

The surface nanotexture and crystal lattice of the surface sulfurized α-$Fe_2O_3$ nanorods were further examined by transmission electron microscope (TEM). It is clear that the α-$Fe_2O_3$ nanorods show diameter almost the same after surface sulfurization

(Fig. 2c and d), corresponding well with the SEM observations. In comparison to the bare α-$Fe_2O_3$ nanorods with clean surface and continuous lattice of d-spacing of 0.25 nm assigned to (1 1 0) plane of α-$Fe_2O_3$ [48] (Fig. 2e), the surface sulfurized α-$Fe_2O_3$ nanorods (Fig. 2f) show surface more rough, and on the nanorod surface some nanocrystallites different from α-$Fe_2O_3$ randomly exist, which could be indexed by the d-spacings of 0.26 and 0.38 nm assigned to the (1 1 2) and (1 0 2) planes of FeS (JCPDS No. 89–6926) [49], respectively. Energy-dispersive spectroscopy (EDS) mapping of Fe-S(0.2) (Fig. S6 online) indicates that S is uniformly distributed over the entire nanorod. Together with XPS analysis, the TEM observations demonstrate the successful surface sulfurization of α-$Fe_2O_3$ nanorods through the facile TAA solution treatment and thus the formation of sulfurized species at the surface of α-$Fe_2O_3$ nanorods.

It is clear that the S element has been incorporated in α-$Fe_2O_3$ as analyzed above. To reveal the effect of the introduced S species on the electronic structures of these surface sulfurized α-$Fe_2O_3$ nanorods, synchrotron x-ray absorption spectroscopy (XAS) at Fe L-edge, O K-edge and S K-edge were conducted. Fig. 3a presents Fe L-edge, which is originated from the electron transition from Fe 2p core level to the Fe 3d unoccupied states. All spectra show a predominant peak with a shoulder-like feature which corresponds to Fe 3d($t_{2g}$) and Fe 3d($e_g$), respectively. Clearly, the bare α-$Fe_2O_3$ nanorods exhibit higher peak intensity compared with the surface sulfurized α-$Fe_2O_3$ nanorods, which indicates that the electronic structure of the α-$Fe_2O_3$ nanorods is strongly altered by surface sulfurization. After surface sulfurization, Fe may gain some charges, probably attributed to the introduced S with less electronegativity than O, and then the electron tends to move back to Fe with Fe-S formed. The well-resolved pre-peaks of O K-edge that are resulted from hybridized O 2p-Fe 3d($t_{2g}$) and O 2p-Fe 3d($e_g$) states are shown in Fig. 3b. The areas under peak A and peak B are associated with the intensity of unoccupied O 2p-Fe 3d($t_{2g}$) and O 2p-Fe 3d($e_g$) states, respectively. The ratio of the area (peak A/peak B) suggests the amount of Fe 3d($t_{2g}$) states and Fig. 3e depicts how this value changes depending on the increasing TAA concentrations for surface sulfurization treatment. Clearly, all surface sulfurized α-$Fe_2O_3$ nanorods have less amount of Fe 3d($t_{2g}$) states compared with bare α-$Fe_2O_3$ nanorods, which is consistent with Fig. 3a. Notably, as the TAA concentration is increased, the Fe 3d($t_{2g}$) is decreased and has lowest value in Fe-S(0.2). Surprisingly, as further increasing TAA concentration, the Fe 3d($t_{2g}$) is increased for the obtained Fe-S(0.5). This abnormal evolution is further verified by looking into the change of Fe 3d($t_{2g}$) and Fe 3d($e_g$) states of Fe-S(0.2) and Fe-S(0.5), with the intensity of Fe 3d($t_{2g}$) states higher and Fe 3d($e_g$) states lower in Fe-S(0.5) than in Fe-S(0.2), as shown in the magnified Fe L-edge spectra (Fig. 3c). These analytical results indicate that the surface sulfurization treatment causes charge redistribution in α-$Fe_2O_3$ nanorods with S species introduced and Fe 3d($t_{2g}$) gains some charges. However, when the TAA concentration for surface sulfurization is too high, the electron back donation is observed from Fe 3d($t_{2g}$) states in Fe-S(0.5), possibly due to the excessive introduction of S species. Fig. 3d presents the S K-edge which probes the electron transition from S 1s to 3p states. A strong feature located at 2481.5 eV depicts the sulfate species [50] introduced to α-$Fe_2O_3$ nanorods, and meanwhile reducing sulfur species have weak features located at 2471.3 and 2472.7 eV [50]. These observations evidence the introduction of the multi-state S species (Fe-$S_x$-$O_y$) into the surface of α-$Fe_2O_3$ nanorods, corresponding well with the XPS analysis and TEM images. Notably, the intensity of S K-edge does not show systematical trend with the TAA concentrations for sulfurization treatment. Thus, to track the electron redistribution, the area under S K-edge is estimated (Fig. 4e). Interestingly, the area under S K-edge has opposite tendency with the amount of unoccupied Fe 3d($t_{2g}$) states, strongly suggesting that charge transfer occurs between α-$Fe_2O_3$ and the introduced S species, and this charge transfer channel is even obvious in Fe-S(0.2).

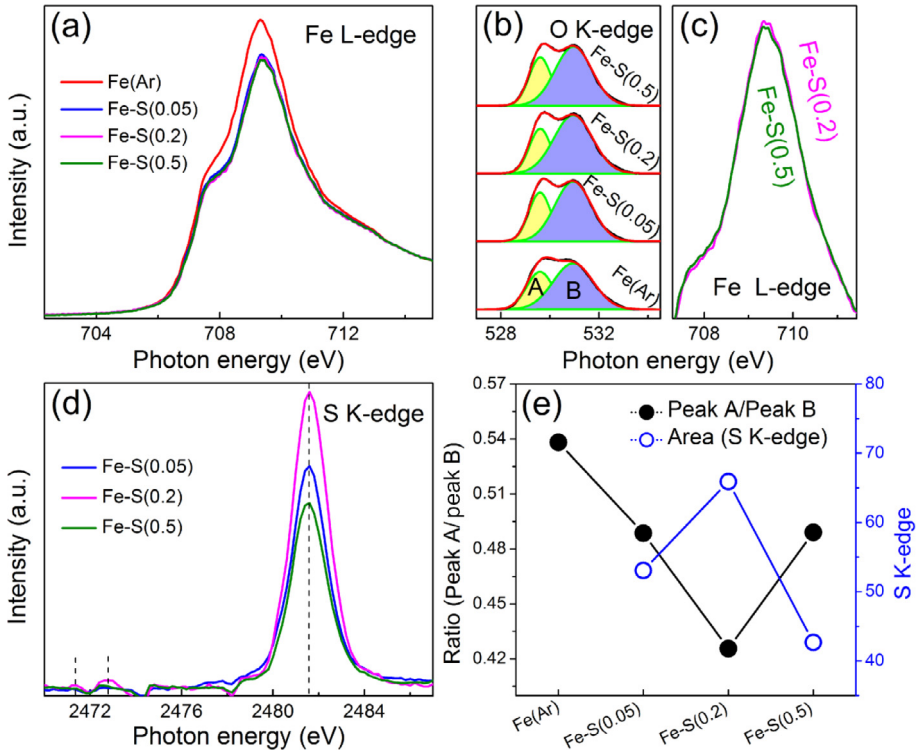


**Fig. 3.** (Color online) XAS spectra at (a) Fe L-edge, (b) O K-edge, and (d) S K-edge. (c) XAS spectra of Fe-S(0.2) and Fe-S(0.5) at magnified Fe L-edge. (e) The ratio of area (peak A/peak B) of Fe(Ar), Fe-S(0.05), Fe-S(0.2), and Fe-S(0.5).

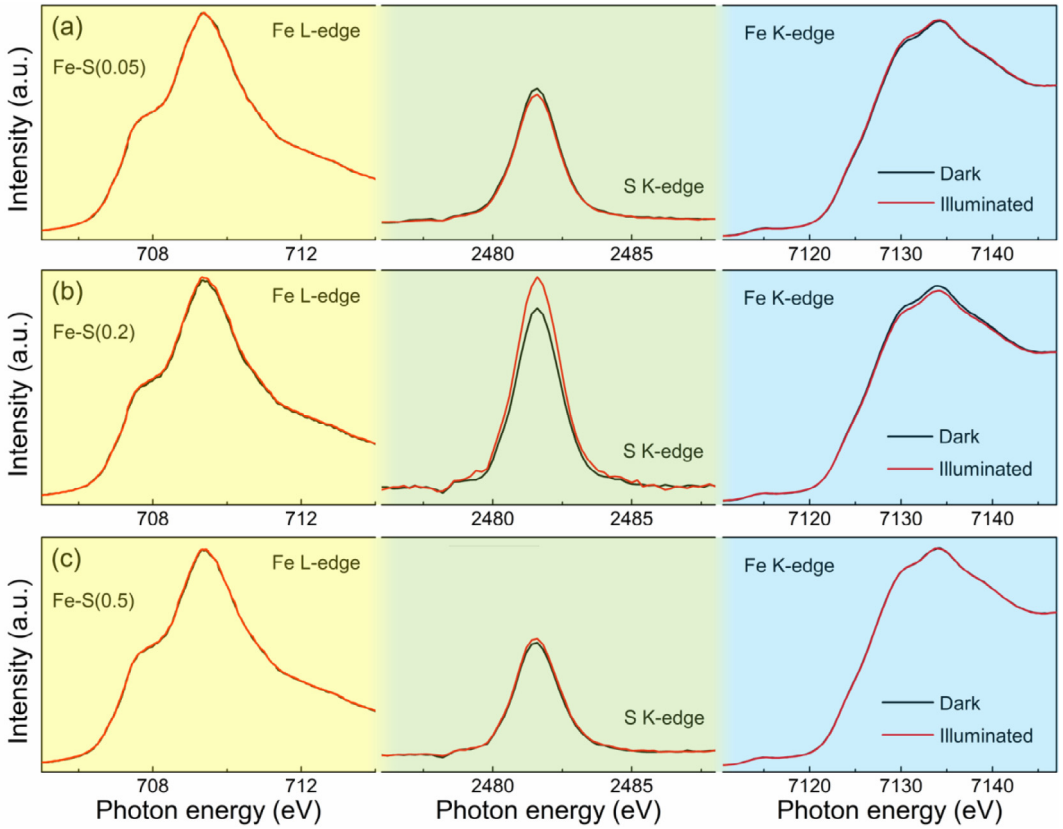


**Fig. 4.** (Color online) XAS spectra of (a) Fe-S(0.05), (b) Fe-S(0.2), and (c) Fe-S(0.5) at Fe L-edge, S K-edge, and Fe K-edge under the dark and illumination conditions.

To further elucidate the charge transfer processes in these surface sulfurized α-$Fe_2O_3$ nanorods from the viewpoint of electronic structure, in situ XAS was conducted. Fig. 4 presents the XAS at Fe L-edge, S K-edge and Fe K-edge of Fe-S(0.05) (Fig. 4a), Fe-S(0.2) (Fig. 4b), and Fe-S(0.5) (Fig. 4c) in the dark (black curve) and under light irradiation (red curve). As presented in Fig. 4a, it is clear that nearly no difference can be seen in the Fe L-edge in the dark and under light irradiation for Fe-S(0.05), which suggests that there might be rapid electron-hole recombination and thus there is very few photogenerated electrons can be excited and populated in the conduction band. However, the peak intensity of S K-edge (Fe K-edge) slightly decreases (increases) as solar light is turned on, implying there is a charge transfer pathway formed in α-$Fe_2O_3$ with S species introduced. Considering the Fe K-edge is more bulk sensitive than Fe L-edge, the charge transfer is likely to be from inner Fe to S site. Notably, both Fe K-edge and Fe L-edge in Fe-S (0.2) are varied in the dark and under light irradiated conditions, as shown in Fig. 4b. This suggests that the charge transfer ability increases not only in the bulk but also in the surface region for Fe-S(0.2) obtained by optimizing the TAA concentration for sulfurization treatment. Interestingly, under the light irradiation, the peak intensity of Fe K-edge (Fe L-edge and S K-edge) is decreased (are increased) compared with that in the dark condition, strongly implying that the hole is migrated from inner region to surface where the Fe-$S_x$-$O_y$ species is formed. Above analytical results indicate the introduction of S species in α-$Fe_2O_3$ nanorods could enrich the charge charrier density and also facilitate the charge transfer ability in the bulk for Fe-S(0.05) and even in both bulk and surface region for Fe-S(0.2). However, for Fe-S(0.5), slight spectral evolution could be revealed only in S K-edge, which implies photoactive sites are reduced significantly, mainly due to too much Fe-$S_x$-$O_y$ species formed in the surface region. This consequence could be attributable to the fact that there is electron back donated from Fe site to S site as increasing the TAA concentrations from Fe-S (0.2) to Fe-S(0.5), as depicted in Fig. 3c–e. This electron back donation leads to less electron density at Fe site and thus less charge carriers can be photogenerated and separated, decreasing the charge transfer probability.

The PEC activities of the obtained α-$Fe_2O_3$ photoanodes were measured by recording the photocurrent density on the dependence of the increasing applied potentials, as shown in Fig. 5a. The bare α-$Fe_2O_3$ photoanodes, both Fe(Air) and Fe(Ar), show negligible photocurrent density. This PEC incompetence was previously reported for the α-$Fe_2O_3$ nanorods grown in aqueous solution and annealed at relatively low temperature (e.g., <600 °C), which always need a high temperature annealing to activate PEC performance [51,52]. Surprisingly, the surface sulfurized α-$Fe_2O_3$ nanorods show remarkable PEC performances for solar water splitting. With TAA concentrations optimized for sulfurization treatment, the highest photocurrent density could reach 0.46 mA $cm^{-2}$ at 1.23 V vs. RHE for Fe-S(0.2), even though the annealing temperature is 550 °C as low. The PEC stability of photoanode is vital for practical applications in the future. Fig. 5b shows that the photocurrent density of Fe-S(0.2) keeps almost unchanged during 10 h PEC reaction. No significant change happens to the XPS S 2p peaks after the 10 h photostability test (Fig. S7 online), and moreover, no sulfur oxidation or reduction peaks appear during cyclic voltammetry (CV) tests (Fig. S8 online), which together indicate the good stability of the surface sulfurized α-$Fe_2O_3$ photoanodes for PEC reaction. Encouragingly, the surface sulfurized α-$Fe_2O_3$ nanorods show superior PEC performance for solar water splitting, in comparison with most α-$Fe_2O_3$ based composite photoanodes annealed at the same low-temperature (550 °C) as shown in Table S1 (online).

The electrochemically active surface area (ECSA) [25] determined by the electrochemical double-layer capacitances ($C_{dl}$) at

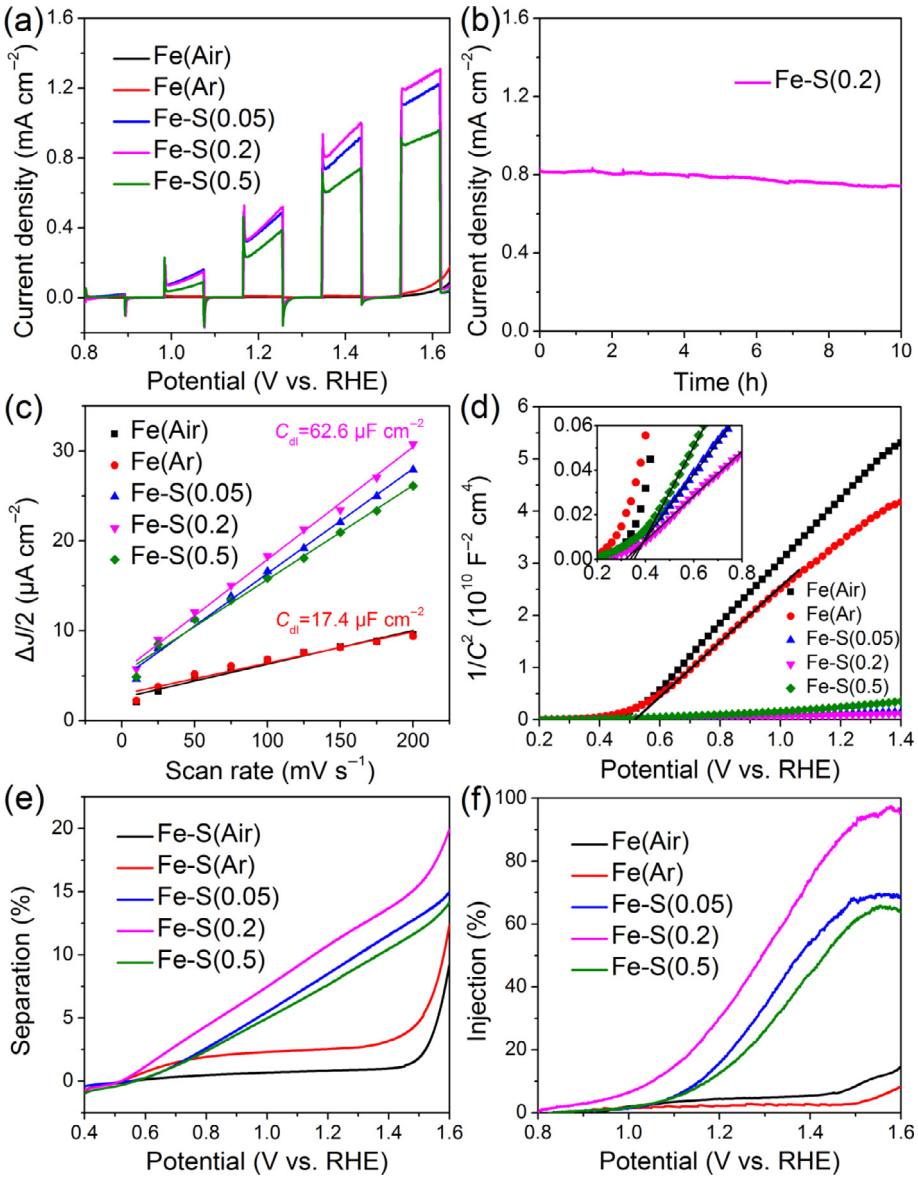


**Fig. 5.** (Color online) (a) Chopped light *J-V* curves; (b) *I-t* curve of Fe-S(0.2) recorded at 1.4 V vs. RHE; (c) The current density variation (Δ*J*/2) as a function of scan rate plotted at the sweep potential range from 0.9 to 1.1 V vs. RHE; (d) Mott-Schottky plots; (e) Bulk charge separation efficiency and (f) surface charge injection efficiency of all photoanodes.

the electrode/electrolyte interface is usually evaluated to estimate the surface active sites for electrochemical reactions. Depending on the CV curves (Fig. S9 online), the linear fitting of half of the current density variation (Δ*J*/2) against scan rates (Fig. 5c) was plotted to extract the measured $C_{dl}$, which were calculated to be 17.4, 58.4, 62.6 and 52.4 μF cm$^{-2}$ for Fe(Ar), Fe-S(0.05), Fe-S(0.2) and Fe-S (0.5), respectively [31]. The highest $C_{dl}$ value achieved for Fe-S (0.2) is about 3.6 times that of Fe(Ar), indicating its largest ECSA. This implies that the introduction of Fe-$S_x$-$O_y$ species by surface sulfurization may offer more active sites for efficient surface water oxidation reactions, thus greatly increase the photocurrent densities, as further supported by EIS analysis in the following discussion. The reduced ECSA for Fe-S(0.5) should be related to the electron back donation leading to less electron density at Fe site as evidenced by XAS results.

To elucidate the effects of surface sulfurization on the electronic properties of α-$Fe_2O_3$ photoanodes for improved PEC activity, the Mott-Schottky (M–S) measurements were carried out at 1 kHz frequency in dark under considering the ECSA. As plotted in Fig. 5d, the positive slopes for all the α-$Fe_2O_3$ photoanodes indicate the n-type nature of semiconductors. These slopes from M–S plots which have a linear relationship, were further used to estimate the carrier density ($N_{d,\,true}$) in semiconductors (see Experimental section), with the calculated $N_{d,\,true}$ values of all the photoanodes shown in Table S2 (online). Obviously, surface sulfurization greatly increases $N_{d,\,true}$ by 2 orders of magnitude as compared with Fe(Ar), which would increase the electric conductivity and then improve the charge transfer ability in the bulk of α-$Fe_2O_3$, as induced by the S incorporation during sulfurization treatment. Considering the short hole diffusion length (usually 2–4 nm) of hematite, only a small part of photogenerated holes can arrive at the electrode surface. Then, the narrowed space charge (depletion) layer width ($W_{sc}$) would benefit holes transfer through the depletion region and decrease the charge carrier recombination. It could be noticed that the $W_{sc}$ was much narrowed (from 9.0 nm for Fe(Ar) to 2.7 nm for Fe-S (0.2), Table S2 online) after surface sulfurization. Therefore, the introduced Fe-$S_x$-$O_y$ species could accelerate the hole transfer through the electrode/electrolyte interface, which should be

responsible for the improved PEC activity, by ruling out the possibility of the formed n-n junction contributing to the much improved charge separation ability (Figs. S10, S11 and Table S3 online).

To further evaluate the charge transfer processes in α-$Fe_2O_3$ nanorod photoanodes, the charge carrier separation and injection efficiencies ($\eta_{separation}$ and $\eta_{injection}$) were quantified (see Experimental section). Fig. 5e presents the charge separation efficiency of the bare and surface sulfurized α-$Fe_2O_3$ nanorod photoanodes, which tells that surface sulfurization can increase the charge separation efficiency of α-$Fe_2O_3$ to some extent, owing to enhanced bulk charge transfer ability as evidenced by M–S and XAS analysis. For example, the charge separation efficiency at 1.23 V vs. RHE was increased from only ~2.5% for Fe(Ar) to ~11.5% for Fe-S(0.2) with TAA concentrations optimized. In addition, with the applied voltage increasing, the charge separation efficiencies of surface sulfurized α-$Fe_2O_3$ photoanodes was extremely increased, due to the widened depletion layer. However, even the best charge separation efficiency is still very low (<15% at 1.23 V vs. RHE), indicating that charge separation remains as one of the significant limitations of PEC activity, due to the instinctive poor bulk electric conductivity of α-$Fe_2O_3$ [53]. Therefore, it could be deduced that the great PEC enhancement should preferably depend on the increased surface charge injection efficiency, as plotted in Fig. 5f. Clearly, surface sulfurization could remarkably increase the charge injection efficiency at 1.23 V vs. RHE from only ~1% for Fe(Ar) to ~38% for Fe-S(0.2), demonstrating the greatly reduced surface hole accumulation and much accelerated water oxidation reaction kinetics as induced by surface sulfurization. This deduction could be supported by the in-situ XAS analysis that the Fe-$S_x$-$O_y$ species at the surface of α-$Fe_2O_3$ accelerate charge transfer ability in the surface region, especially for Fe-S(0.2).

As shown in Fig. 6a, the incident photon to current conversion efficiency (IPCE) values for bare α-$Fe_2O_3$ photoanodes, e.g., Fe(Ar), are extremely low, meaning the poor PEC properties of the inactivated α-$Fe_2O_3$ nanorods. In sharp contrast, the Fe-S(0.2) film shows obviously enhanced IPCEs at the wavelengths ranging from 300 to 650 nm, with IPCE value reaching 5.6% at 400 nm, which again evidences the great PEC enhancement induced by surface sulfurization. Given the very similar optical absorption properties of bare and surface sulfurized α-$Fe_2O_3$ photoanodes (Fig. S12 online), the enhanced PEC properties are not likely related to the optical absorption, but more likely other altered intrinsic characteristics, including promoted charge transfer processes and accelerated surface reaction kinetics.

To further understand the charge transfer processes at the electrode/electrolyte interface, electrochemical impedance spectroscopy (EIS) analysis conducted at 1.23 V vs. RHE under illumination was employed for all the photoanodes with results shown in Fig. 6b. A 2-RC equivalent circuit model [54,55] was applied to fit the Nyquist plots (Fig. S13 online), with its parameters summarized in Table S3 (online). As compared to the bare α-$Fe_2O_3$ photoanodes, all the surface sulfurized α-$Fe_2O_3$ nanorod photoanodes show reduced bulk charge transfer resistance ($R_1$), indicating the improved bulk charge transfer process, which should be benefited from the improved electrical conductivity due to the increased carrier density, as evidenced by the M–S and XAS results. Furthermore, the decreased interface charge transfer resistance ($R_2$) and the increased Helmholtz capacitance ($CPE_2$) reveal the promoted charge transfer processes through the electrode/electrolyte interface for the accelerated water oxidation kinetics [56], as induced by the effective surface sulfurization modification. It could be thus assumed that the efficient charge transfer process at the electrode/electrolyte interface largely determines the improved PEC performances of the surface sulfurized α-$Fe_2O_3$ nanorod photoanodes. However, the excessive sulfurization may reduce the photoactive sites and thus block holes transfer across the electrode/electrolyte interface, as indicated by the increased $R_2$ for Fe-S(0.5), which gives rise to the reduced PEC activity. All these electrochemical observations can be well evidenced by the XAS analysis. Together with the above (photo)electrochemical analysis, it can be then concluded that the surface sulfurization treatment could improve the charge transfer ability to some extent by increasing the charge carrier density and decreasing charge transfer resistance in bulk, and meanwhile largely promote the electrode/electrolyte interface charge transfer processes for the accelerated surface water oxidation reaction kinetics by improving the charge transfer ability in the surface region.

Based on the experimental results and analysis above, charge carrier transfer processes were schemed to explain how the surface sulfurization can effectively increase the PEC performance of α-$Fe_2O_3$ photoanodes as shown in Fig. 7. Due to the existence of surface defect states and the sluggish water oxidation reaction kinetics of α-$Fe_2O_3$, the photogenerated holes are very likely trapped and recombined at the surface of the photoanode, which limits the photogenerated hole transfer from surface to the electrolyte for the following water oxidation reaction [57,58], leading to the poor PEC performance. In comparison, after surface sulfurization, the bulk charge recombination is inhibited due to the increased electrical conductivity as revealed by the increased carrier density and then the reduced bulk charge transfer resistance; and more importantly, the charge transfer processes at the electrode/electrolyte interface are greatly promoted, which can be expected from the greatly reduced interface charge transfer resistance. In addition, the surface active sites increased by the surface introduction of Fe-$S_x$-$O_y$ species enable efficient photogenerated hole transfer through the photoanode/electrolyte interface to inject into the electrolyte, thus accelerating the water oxidation reaction kinetics. Together with XAS analysis evidencing that the introduced Fe-$S_x$-$O_y$ species facilitating

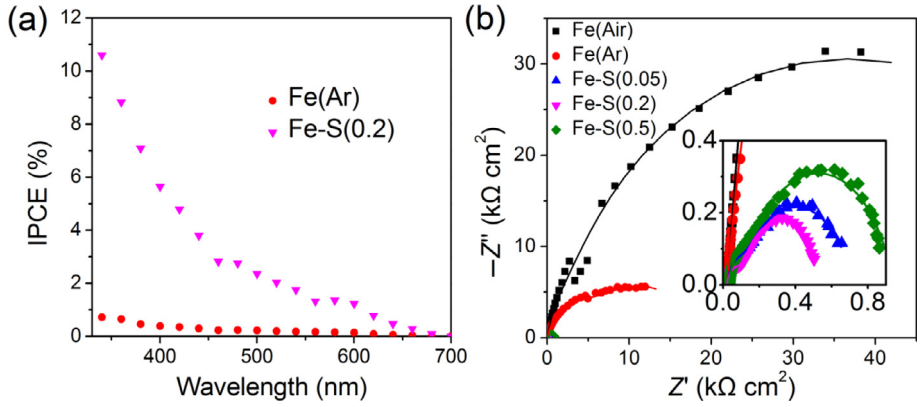


**Fig. 6.** (Color online) (a) IPCE profiles collected at 1.23 V vs. RHE; (b) Nyquist plots of all photoanodes under illumination.

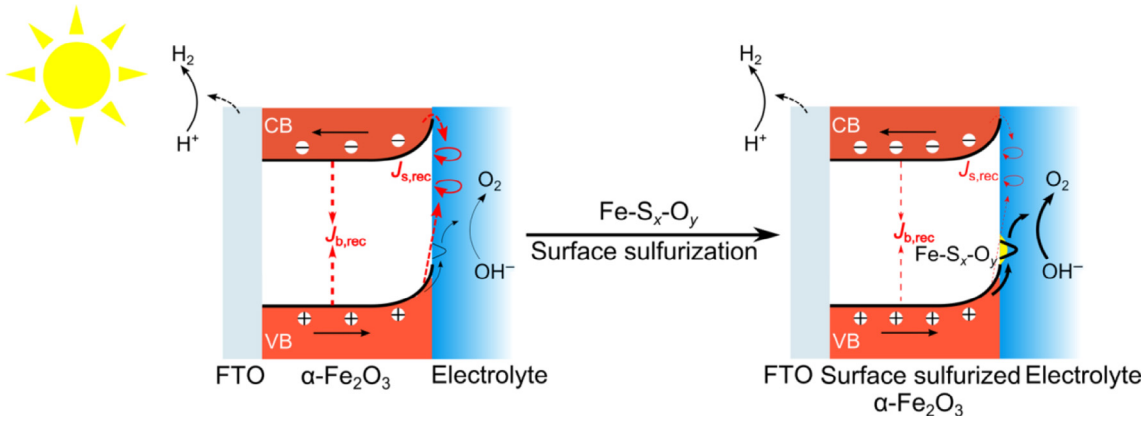


**Fig. 7.** (Color online) Diagrams of charge transfer process in the bulk and at the surface of α-$Fe_2O_3$ before and after surface sulfurization. CB: conduction band, VB: valence band, $J_{s,rec}$ and $J_{b,rec}$ represent surface and bulk charge carrier recombination, respectively.

charge transfer ability in both bulk and surface regions, it is then explainable that surface sulfurization can effectively promote charge carrier separation and transfer processes as well as accelerate water oxidation reaction kinetics, which synergistically improves the PEC performance of α-$Fe_2O_3$ photoanodes for solar water splitting. This surface sulfurization modification approach provides an alternative pathway towards efficient PEC water oxidation on α-$Fe_2O_3$ photoanodes by enhancing bulk and surface charge transfer ability as well as alleviating hole accumulation and recombination at the surface, which can be extended to other metal oxide semiconductor photoanodes in other fields of solar energy conversion.

## 4. Conclusions

In summary, surface sulfurized α-$Fe_2O_3$ nanorod photoanodes were successfully fabricated via a facile aqueous solution approach followed by a low-temperature (<600 °C) annealing process. After surface sulfurization, the α-$Fe_2O_3$ nanorod photoanodes show remarkable enhancement in PEC performances for water oxidation, with a highest photocurrent density reaching 0.46 mA $cm^{-2}$ at 1.23 V vs. RHE under simulated solar irradiation. It was demonstrated that the great PEC enhancement could be achieved by the surface sulfurization treatment introducing multi-state S species in the surface region of α-$Fe_2O_3$ nanorods, which could increase the charge carrier density and thus enhance the electrical conductivity for improved charge separation in the bulk of α-$Fe_2O_3$ to a certain extent, and extensively reduce the accumulation of photoexcited holes at the surface of the photoanodes and then greatly increase the charge injection efficiency at the electrode/electrolyte interface for accelerated surface water oxidation reaction kinetics. Although the PEC activity is still not high enough and needs further improvement for practical applications, this study demonstrates an effective but facile approach for surface modification of metal oxide photoelectrodes towards high efficiency and low cost solar hydrogen conversion.

## Conflict of interest

The authors declare that they have no conflict of interest.

## Acknowledgments

This work was financially supported by the National Natural Science Foundation of China (21875183, 51672210 and 51888103), the National Program for Support of Top-notch Young Professionals and the "Fundamental Research Funds for the Central Universities".

## Author contributions

L. Mao conducted the experiments and wrote the manuscript. Y.-C. Huang and C.-L. Dong performed the XAS test and data analysis. Y. Fu helped conduct the electrochemical characterizations. S. Shen supervised this study and wrote the manuscript.

## Appendix A. Supplementary data

Supplementary data to this article can be found online at https://doi.org/10.1016/j.scib.2019.07.008.

## References

[1] Liu D, Liu J-C, Cai W, et al. Selective photoelectrochemical oxidation of glycerol to high value-added dihydroxyacetone. Nat Commun 2019;10:1779.
[2] Fujishima A, Honda K. Electrochemical photolysis of water at a semiconductor electrode. Nature 1972;238:37–8.
[3] Hsu S-H, Miao J, Zhang L, et al. An earth-abundant catalyst-based seawater photoelectrolysis system with 17.9% solar-to-hydrogen efficiency. Adv Mater 2018;30:1707261.
[4] Shen S, Chen J, Wang M, et al. Titanium dioxide nanostructures for photoelectrochemical applications. Prog Mater Sci 2018;98:299–385.
[5] Wang Z, Mao X, Chen P, et al. Understanding the roles of oxygen vacancies in hematite-based photoelectrochemical processes. Angew Chem Int Ed 2019;58:1030–4.
[6] Liu D, Liu B. Novel design of photoelectrochemical device by dual $BiVO_4$ photoelectrode with abundant oxygen vacancy. Sci Bull 2018;63:1027–8.
[7] Zeng Q, Li J, Bai J, et al. Preparation of vertically aligned $WO_3$ nanoplate array films based on peroxotungstate reduction reaction and their excellent photoelectrocatalytic performance. Appl Catal B Environ 2017;202:388–96.
[8] Shavorskiy A, Ye X, Karslıoğlu O, et al. Direct mapping of band positions in doped and undoped hematite during photoelectrochemical water splitting. J Phys Chem Lett 2017;8:5579–86.
[9] Shen S, Lindley SA, Chen X, et al. Hematite heterostructures for photoelectrochemical water splitting: rational materials design and charge carrier dynamics. Energy Environ Sci 2016;9:2744–75.
[10] Zhang R, Fang Y, Chen T, et al. Enhanced photoelectrochemical water oxidation performance of $Fe_2O_3$ nanorods array by S doping. ACS Sustain Chem Eng 2017;5:7502–6.
[11] Tang P, Xie H, Ros C, et al. Enhanced photoelectrochemical water splitting of hematite multilayer nanowire photoanodes by tuning the surface state via bottom-up interfacial engineering. Energy Environ Sci 2017;10:2124–36.
[12] Shen S. Toward efficient solar water splitting over hematite photoelectrodes. J Mater Res 2014;29:29–46.
[13] Wang J, Yang J, Zheng Z, et al. The role of thin NiPi film for enhancing solar water splitting performance of Ti doped hematite. Appl Catal B Environ 2017;218:277–86.
[14] Malviya KD, Dotan H, Shlenkevich D, et al. Systematic comparison of different dopants in thin film hematite (α-$Fe_2O_3$) photoanodes for solar water splitting. J Mater Chem A 2016;4:3091–9.
[15] Subramanian A, Gracia-Espino E, Annamalai A, et al. Effect of tetravalent dopants on hematite nanostructure for enhanced photoelectrochemical water splitting. Appl Surf Sci 2018;427:1203–12.
[16] Jeon TH, Bokare AD, Han DS, et al. Dual modification of hematite photoanode by Sn-doping and $Nb_2O_5$ layer for water oxidation. Appl Catal B Environ 2017;201:591–9.

[17] Luo Z, Li C, Liu S, et al. Gradient doping of phosphorus in $Fe_2O_3$ nanoarray photoanodes for enhanced charge separation. Chem Sci 2017;8:91–100.
[18] Shen S, Mao SS. Nanostructure designs for effective solar-to-hydrogen conversion. Nanophotonics 2012;1:31–50.
[19] Wheeler DA, Wang G, Ling Y, et al. Nanostructured hematite: synthesis, characterization, charge carrier dynamics, and photoelectrochemical properties. Energy Environ Sci 2012;5:6682–702.
[20] Fu Y, Cao F, Wu F, et al. Phase-modulated band alignment in CdS nanorod/$SnS_x$ nanosheet hierarchical heterojunctions toward efficient water splitting. Adv Funct Mater 2018;28:1706785.
[21] Liu R, Zheng Z, Spurgeon J, et al. Enhanced photoelectrochemical water-splitting performance of semiconductors by surface passivation layers. Energy Environ Sci 2014;7:2504–17.
[22] Wang M, Wang M, Fu Y, et al. Cobalt oxide and carbon modified hematite nanorod arrays for improved photoelectrochemical water splitting. Chin Chem Lett 2017;28:2207–11.
[23] Yang J, Wang D, Han H, et al. Roles of cocatalysts in photocatalysis and photoelectrocatalysis. Acc Chem Res 2013;46:1900–9.
[24] Ding C, Shi J, Wang Z, et al. Photoelectrocatalytic water splitting: significance of cocatalysts, electrolyte, and interfaces. ACS Catal 2017;7:675–88.
[25] Fan Z, Xu Z, Yan S, et al. Tuning the ion permeability of an $Al_2O_3$ coating layer on $Fe_2O_3$ photoanodes for improved photoelectrochemical water oxidation. J Mater Chem A 2017;5:8402–7.
[26] Chen X, Fu Y, Kong T, et al. Protected hematite nanorod arrays with molecular complex co-catalyst for efficient and stable photoelectrochemical water oxidation. Eur J Inorg Chem 2019;2019:2078–85.
[27] Xi L, Bassi PS, Chiam SY, et al. Surface treatment of hematite photoanodes with zinc acetate for water oxidation. Nanoscale 2012;4:4430–3.
[28] Yang Y, Forster M, Ling Y, et al. Acid treatment enables suppression of electron-hole recombination in hematite for photoelectrochemical water splitting. Angew Chem Int Ed 2016;55:3403–7.
[29] Lan H, Wei A, Zheng H, et al. Boron-passivated surface $Fe^{(IV)}$ defects in hematite for highly efficient water oxidation. Nanoscale 2018;10:7033–9.
[30] Vayssieres L, Beermann N, Lindquist S-E, et al. Controlled aqueous chemical growth of oriented three-dimensional crystalline nanorod arrays: application to iron(III) oxides. Chem Mater 2001;13:233–5.
[31] Wang M, Dong C-L, Huang Y-C, et al. Electronic structure evolution in tricomponent metal phosphides with reduced activation energy for efficient electrocatalytic oxygen evolution. Small 2018;14:1801756.
[32] Shen S, Kronawitter CX, Wheeler DA, et al. Physical and photoelectrochemical characterization of Ti-doped hematite photoanodes prepared by solution growth. J Mater Chem A 2013;1:14498–506.
[33] Steier L, Luo J, Schreier M, et al. Low-temperature atomic layer deposition of crystalline and photoactive ultrathin hematite films for solar water splitting. ACS Nano 2015;9:11775–83.
[34] Yi S-S, Wulan B-R, Yan J-M, et al. Highly efficient photoelectrochemical water splitting: surface modification of cobalt-phosphate-loaded $Co_3O_4/Fe_2O_3$ p-n heterojunction nanorod arrays. Adv Funct Mater 2019;29:1801902.
[35] Dotan H, Sivula K, Grätzel M, et al. Probing the photoelectrochemical properties of hematite ($\alpha$-$Fe_2O_3$) electrodes using hydrogen peroxide as a hole scavenger. Energy Environ Sci 2011;4:958–64.
[36] Zhao X, Feng J, Chen S, et al. New insight into the roles of oxygen vacancies in hematite for solar water splitting. Phys Chem Chem Phys 2017;19:1074–82.
[37] Fu Y, Dong C-L, Zhou Z, et al. Solution growth of Ta-doped hematite nanorods for efficient photoelectrochemical water splitting: a tradeoff between electronic structure and nanostructure evolution. Phys Chem Chem Phys 2016;18:3846–53.
[38] Shen S, Guo P, Wheeler DA, et al. Physical and photoelectrochemical properties of Zr-doped hematite nanorod arrays. Nanoscale 2013;5:9867–74.
[39] Liao A, Chen R, Fan F, et al. Integration of $Fe_xS$ electrocatalysts and simultaneously generated interfacial oxygen vacancies to synergistically boost photoelectrochemical water splitting of $Fe_2O_3$ photoanodes. Chem Commun 2018;54:13817–20.
[40] Du J, Bao J, Fu X, et al. Mesoporous sulfur-modified iron oxide as an effective Fenton-like catalyst for degradation of bisphenol A. Appl Catal B Environ 2016;184:132–41.
[41] Li Y, Yin J, An L, et al. $FeS_2/CoS_2$ interface nanosheets as efficient bifunctional electrocatalyst for overall water splitting. Small 2018;14:1801070.
[42] Fan J, Gu L, Wu D, et al. Mackinawite (FeS) activation of persulfate for the degradation of p-chloroaniline: surface reaction mechanism and sulfur-mediated cycling of iron species. Chem Eng J 2018;333:657–64.
[43] Herbert FW, Krishnamoorthy A, Ma W, et al. Dynamics of point defect formation, clustering and pit initiation on the pyrite surface. Electrochim Acta 2014;127:416–26.
[44] Cabán-Acevedo M, Kaiser NS, English CR, et al. Ionization of high-density deep donor defect states explains the low photovoltage of iron pyrite single crystals. J Am Chem Soc 2014;136:17163–79.
[45] Samad L, Cabán-Acevedo M, Shearer MJ, et al. Direct chemical vapor deposition synthesis of phase-pure iron pyrite ($FeS_2$) thin films. Chem Mater 2015;27:3108–14.
[46] Shen S, Lindley SA, Dong C-L, et al. Enhancing solar-driven water splitting with surface-engineered nanostructures. Sol RRL 2019. https://doi.org/10.1002/solr.201800285.
[47] Li Q, Bian J, Zhang N, et al. Loading $Ni(OH)_2$ on the Ti-doped hematite photoanode for photoelectrochemical water splitting. Electrochim Acta 2015;155:383–90.
[48] Ahn H-J, Goswami A, Riboni F, et al. Hematite photoanode with complex nanoarchitecture providing tunable gradient doping and low onset potential for photoelectrochemical water splitting. Chem Sus Chem 2018;11:1873–9.
[49] Zhang C, Deng L, Zhang P, et al. Electrospun FeS nanorods with enhanced stability as counter electrodes for dye-sensitized solar cells. Electrochim Acta 2017;229:229–38.
[50] Guo H, Fu Q, Zhang L, et al. Sulfur K-edge XAS study of sulfur transformation behavior during pyrolysis and co-pyrolysis of biomass and coals under different atmospheres. Fuel 2018;234:1322–7.
[51] Annamalai A, Shinde PS, Subramanian A, et al. Bifunctional $TiO_2$ underlayer for $\alpha$-$Fe_2O_3$ nanorod based photoelectrochemical cells: enhanced interface and $Ti^{4+}$ doping. J Mater Chem A 2015;3:5007–13.
[52] Qiu P, Yang H, Yang L, et al. Solar water splitting with nanostructured hematite: the role of annealing-temperature. Electrochim Acta 2018;266:431–40.
[53] Abel AJ, Patel AM, Smolin SY, et al. Enhanced photoelectrochemical water splitting via SILAR-deposited Ti-doped hematite thin films with an FeOOH overlayer. J Mater Chem A 2016;4:6495–504.
[54] Kim DH, Andoshe DM, Shim Y-S, et al. Toward high-performance hematite nanotube photoanodes: charge-transfer engineering at heterointerfaces. ACS Appl Mater Interfaces 2016;8:23793–800.
[55] Han H, Kment S, Karlicky F, et al. Sb-doped $SnO_2$ nanorods underlayer effect to the $\alpha$-$Fe_2O_3$ nanorods sheathed with $TiO_2$ for enhanced photoelectrochemical water splitting. Small 2018;14:1703860.
[56] Ding D, Dong B, Liang J, et al. Solvothermal-etching process induced Ti-doped $Fe_2O_3$ thin film with low turn-on voltage for water splitting. ACS Appl Mater Interfaces 2016;8:24573–8.
[57] Klahr B, Gimenez S, Fabregat-Santiago F, et al. Electrochemical and photoelectrochemical investigation of water oxidation with hematite electrodes. Energy Environ Sci 2012;5:7626–36.
[58] Hajibabaei H, Schon AR, Hamann TW. Interface control of photoelectrochemical water oxidation performance with $Ni_{1-x}Fe_xO_y$ modified hematite photoanodes. Chem Mater 2017;29:6674–83.

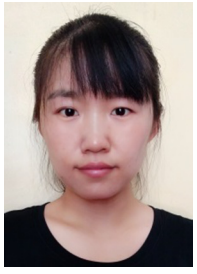

Lianlian Mao is currently pursuing a Ph.D. degree under the supervision of Prof. Shaohua Shen at International Research Center for Renewable Energy, State Key Laboratory of Multiphase Flow in Power Engineering, Xi'an Jiaotong University. Her research interests focus on the modification of metal oxide nanostructures for efficient photoelectrochemical water splitting.

Chung-Li Dong has a Ph.D. degree in Physics (2004, Tamkang University) and conducted postdoctoral research work at the Institute of Physics, Academia Sinica, Taiwan, and at Advanced Light Source, Lawrence Berkeley National Laboratory from 2005–2009. He is currently an Associate Professor at Tamkang University. His research work focuses on the synchrotron in situ/-operando spectroscopic studies of advanced and energy materials.

Shaohua Shen is currently a professor at Xi'an Jiaotong University. He obtained his Ph.D. degree in thermal engineering in 2010 from Xi'an Jiaotong University. During 2008–2009 and 2011–2012, he worked as a guest researcher at Lawrence Berkeley National Laboratory and a postdoctoral researcher at the University of California at Berkeley. His research interests include photocatalytic and photoelectrochemical solar energy conversion.